Frozen reaction fronts in steady flows: A burning-invariant-manifold perspective

John R. Mahoney,[1,*] John Li,[2,3] Carleen Boyer,[4] Tom Solomon,[4] and Kevin A. Mitchell[2,†]
[1]*University of California, Davis, California 95616, USA*
[2]*University of California, Merced, California 95344, USA*
[3]*University of Southern California, Los Angeles, California 90089, USA*
[4]*Bucknell University, Lewisburg, Pennsylvania 17837, USA*
(Received 27 March 2015; revised manuscript received 20 August 2015; published 7 December 2015)

The dynamics of fronts, such as chemical reaction fronts, propagating in two-dimensional fluid flows can be remarkably rich and varied. For time-invariant flows, the front dynamics may simplify, settling in to a steady state in which the reacted domain is static, and the front appears "frozen." Our central result is that these frozen fronts in the two-dimensional fluid are composed of segments of *burning invariant manifolds*, invariant manifolds of front-element dynamics in $xy\theta$ space, where θ is the front orientation. Burning invariant manifolds (BIMs) have been identified previously as important local barriers to front propagation in fluid flows. The relevance of BIMs for frozen fronts rests in their ability, under appropriate conditions, to form global barriers, separating reacted domains from nonreacted domains for all time. The second main result of this paper is an understanding of bifurcations that lead from a nonfrozen state to a frozen state, as well as bifurcations that change the topological structure of the frozen front. Although the primary results of this study apply to general fluid flows, our analysis focuses on a chain of vortices in a channel flow with an imposed wind. For this system, we present both experimental and numerical studies that support the theoretical analysis developed here.

DOI: 10.1103/PhysRevE.92.063005 PACS number(s): 47.70.Fw, 82.40.Ck, 47.10.Fg

I. INTRODUCTION: REACTING FLOWS AND FROZEN FRONTS

The evolution of an autocatalytic reaction $A + B \rightarrow 2A$ in a spatially extended system is characterized by the propagation of reaction fronts that separate the species A and B. The motion of these fronts is well understood for reaction-diffusion systems in the absence of any substrate flow. The effects of fluid motion on fronts in the more general *advection-reaction-diffusion* system have only recently received significant attention. This is somewhat surprising, given the applicability of advection-reaction-diffusion to a wide range of systems, including microfluidic chemical reactors [1], plasmas [2], the dynamics of ecosystems in the oceans (e.g., plankton blooms) [3], cellular- and embryonic-scale biological processes [4,5], and the propagation of diseases in society [6]. It has been recently proposed that the motion of reaction fronts in fluid flows may be dominated by the presence of *burning invariant manifolds* (BIMs), which act as one-way barriers to advancing fronts [7,8]. The existence of BIMs and their function as one-way barriers has been verified experimentally in time-independent and time-periodic vortex chain flows, as well as two-dimensional (2D) disordered vortex flows [9].

Experiments have shown that reaction fronts tend to pin to vortex structures in the presence of an imposed wind [10]. These fronts neither propagate forward against the wind nor are blown backwards, but remain "frozen." This behavior is surprisingly robust, occurring over more than an order of magnitude of wind speeds and a variety of underlying flows ranging from confined vortex chains to extended, spatially random flows. Figure 1 shows a sequence of images from experiments showing the evolution of a triggered, autocatalytic reaction front in a vortex chain with wind. The front eventually stabilizes and remains fixed for the duration of the experiment.

In this paper, we use the theory of BIMs to characterize these *frozen fronts*. Frozen fronts occur when a BIM spans the entire width of the system with no changes in blocking direction, or when there is a combination of overlapping BIMs, with the same blocking directions, that together span the system. In either of these situations, the shape of the frozen front is determined by the shape of the BIMs responsible. We illustrate the creation of frozen fronts and changes in their structure by increasing the wind applied to a canonical base flow (the alternating vortex chain) with a propagating chemical reaction. We present both experimental and numerical studies of this system.

This paper is organized as follows. We begin in Sec. II by presenting experiments involving reaction fronts in a particular quasi-two-dimensional fluid flow: the "windy alternating vortex chain." The images in this section illustrate the behavior of frozen fronts under an imposed wind of various strengths. Section III recalls some basic aspects of *burning invariant manifolds* (BIMs), geometric structures that govern the progress of fronts in fluid flows, including the three-dimensional dynamics of front elements and fixed points of this system. Next, Sec. IV connects the previous two sections by showing that frozen fronts are composed of BIM segments. Section V considers frozen fronts in a numerical model of the experimental flow. It parallels Sec. II by increasing the applied wind and observing the resulting changes in the frozen fronts. Here, we discuss in detail the various frozen front topologies and the dynamical systems mechanism underlying the transitions which connect them. There are two appendixes. Appendix A introduces a two-dimensional invariant surface of "sliding fronts," which is used to prove several key results in the paper. Then, Appendix B establishes the stability condition that frozen fronts must satisfy.

*jrmahoney@ucdavis.edu
†kmitchell@ucmerced.edu

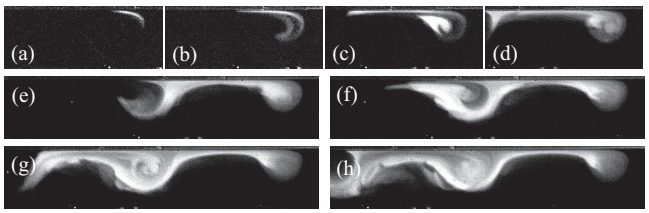

FIG. 1. Sequence showing the evolution of a triggered reaction front. The maximum fluid vortex speed (in the absence of wind) is $U = 1.4$ mm/s, and the wind speed is $V_w = 0.90$ mm/s (leftward). The cell width (vertical dimension in the images) is 1.9 cm. The images in the sequence are separated by 10 s.

II. EXPERIMENTS: WINDY ALTERNATING VORTEX CHAIN FLOW

The alternating vortex chain fluid flow has been the subject of much study, both theoretical and experimental. It has been used as a model of a two-dimensional cross section of Rayleigh-Bénard (thermal) convection [11–14] and Taylor-Couette vortices [15], and can be used to model vortex chains and streets in oceanic and atmospheric flows [16,17]. The alternating vortex chain has been used to study enhancement of long-range, fluid transport in cellular flows [18–21]. More recently, it has been used repeatedly in studies of chemical front propagation in advection-reaction-diffusion systems [7,22–26]. Here, we modify this flow by adding a uniform "wind," creating the *windy alternating vortex chain* [10].

A. Experimental setup

The experiments are conducted in a quasi-2D flow composed of a chain of vortices in a thin (2 mm) fluid layer. The flow is produced using a magnetohydrodynamic forcing technique, as shown in Fig. 2. A chain of permanent 1.9-cm-diameter Nd-Fe-Bo magnets sits below the fluid layer, thereby imposing a spatially varying magnetic field. An electric current is passed through this electrolytic fluid, generating Lorentz forces on the fluid. In conjunction with rigid, plastic sidewalls that bound the region of interest, the result is an alternating chain of well-controlled vortices. The magnets are mounted on a translation stage; motion of the translation stage results in motion of the magnets and, consequently, the fluid vortices. In these experiments, we move the magnets (and the vortices) with a constant speed V_w. In the reference frame moving with the magnets, the flow is a stationary chain of vortices with an imposed, uniform wind of speed V_w.

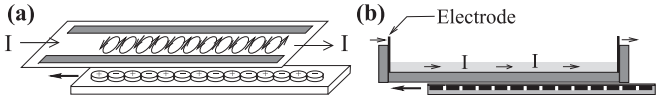

FIG. 2. Experimental apparatus. (a) Exploded view of alternating fluid vortices above array of magnets. Two acrylic strips bound the fluid domain, which measures 1.9 cm × 26.7 cm, with 14 vortices. Current through fluid induces Lorenz force. (b) Side view of the apparatus. A 2-mm-thick layer of an electrolytic fluid is contained in an acrylic box. The chain of Nd-Fe-Bo magnets moves on a translation stage below the box.

The fronts are produced in the experiments with the excitable, ferroin-catalyzed Belousov-Zhabotinsky chemical reaction [27,28]. At the beginning of an experimental run, the ferroin indicator in the solution is in its reduced (orange) state. A reaction is then triggered by briefly dipping a silver wire into the fluid. The silver oxidizes the ferroin in its vicinity, changing the local indicator to a blue-green color. The oxidized indicator in turn oxidizes the ferroin of *its* neighbors, resulting in a blue-green reaction front that steadily propagates outward from the trigger point with a roughly constant propagation speed V_0. For all experiments presented in this article, the propagation speed is $V_0 = 0.07$ mm/s. The front is a pulselike front; behind the leading edge of the front, the reaction relaxes back to its reduced (orange) state and can be re-triggered. Previous studies [24–26] have shown that the *leading edge* of these pulselike fronts exhibits the same propagation dynamics as the *leading edge* of a burn-type reaction. (Burn-type reactions do not relax back, rather $A + B \rightarrow 2A$ and stays that way.) That is, what happens behind the front does not affect the evolution of the front itself.

B. Experimental results

We focus on the behavior of the leading edge of the reaction front that propagates *against* the imposed wind. (In the laboratory frame, these fronts propagate in the direction of the imposed motion of the vortex cores.) An example of a typical experiment is shown in Fig. 3. As viewed in the laboratory reference frame [Fig. 3(a)], the front continually propagates in both directions; in the reference frame moving with the vortices [Fig. 3(b)] the rightmost edge of the reaction front converges to a steady-state stationary shape that remains fixed for the duration of the run. From here on, we use the expression "wind" V_w to refer to either the translational speed of the vortices in the laboratory frame or the speed of the uniform wind in the vortex reference frame.

The propagation of a reaction front in the alternating vortex flow in the absence of an imposed wind has been discussed in detail in previous papers [25,26,29,30]. The reaction front is carried around each vortex with the flow and "burns" across the separatrix from one vortex to the next, resulting in

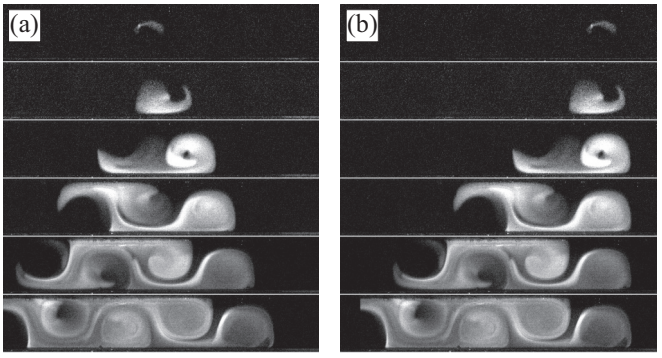

FIG. 3. Sequences showing the evolution of a reaction front in a vortex chain. (a) Laboratory frame, with the vortices moving to the right. (b) Reference frame moving with the vortices. In this frame, the vortices are stationary and a wind blows across the vortices toward the left. $U = 1.4$ mm/s, $V_w = 0.30$ mm/s. Images in the sequences are separated by 20 s.

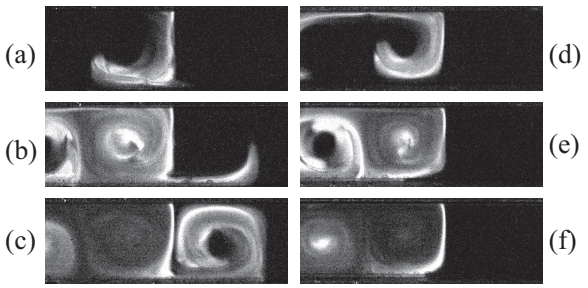

FIG. 4. Two sequences demonstrate front evolution near critical wind speed. The maximum fluid vortex speed (in the absence of wind) is $U = 0.7$ mm/s. For wind value $V_w = 0.085$ mm/s, the front is (a) nearly vertical, (b) finds a small passage into the next right vortex, and (c) fills in the right vortex continuing down the channel. For wind value $V_w = 0.090$ mm/s, the front is (d) nearly vertical, (e) does not find passage to the right, and (f) remains unchanged from (e), a frozen front. The time between images is 40 s in both sequences. Note that there is a small amount of experimental noise that increases the transition slightly above $V_w = V_0 = 0.07$ mm/s.

long-range propagation that is significantly faster than the reaction-diffusion speed V_0 in a static fluid. The long-term average front speed is independent of the initial stimulation.

If a uniform wind $V_w < V_0$ is applied (i.e., the wind speed is smaller than the reaction-diffusion speed), the reaction front still propagates to the right against the wind, although the long-range propagation speed is reduced. At $V_w = V_0$, there is a transition where the front neither advances against the wind nor is blown backwards [10]. Figure 4 shows a sequence for a reaction front triggered in a flow with wind V_w just below V_0 [Figs. 4(a)–4(c)] and V_w just above V_0 [Figs. 4(d)–4(f)]. The shape of the frozen front is not arbitrary; rather, a wide range of initial stimulations will result in fronts that converge onto the same structure. For $V_w = V_0$, the shape of the frozen front corresponds well with the advective separatrix having $V_w = 0$.

As the strength of the imposed wind is increased, the shape of the frozen front evolves considerably. Figure 5 shows time-averaged images of the steady-state reaction fronts for several different wind speeds. With increasing wind speed, the contact point of the frozen front with the upper boundary does not move much. There is also a shift-flip symmetry apparent in Figs. 5(b)–5(g); for every frozen front originating from a contact point there is a flipped version of the same structure originating from a contact point one vortex width leftward. Consequently, for any wind speed, the leading edge of the front could be pinned to any one of these contact points; i.e., any frozen front could be replaced by the same shape, shifted by one vortex and flipped vertically.

The shift-flip symmetry is also relevant to a change in the structure of the frozen front as the wind speed is increased. The front develops a point, or corner, with an apparently discontinuous derivative [Fig. 5(b)]. This point moves leftward for larger and larger wind speeds [Figs. 5(c)–5(g)]. This concave corner first appears near the downwind contact point (one vortex width downwind in Fig. 5(b) and moves away from the channel wall. In this situation, the frozen front is composed of a combination of smooth curves that originate at different contact points.

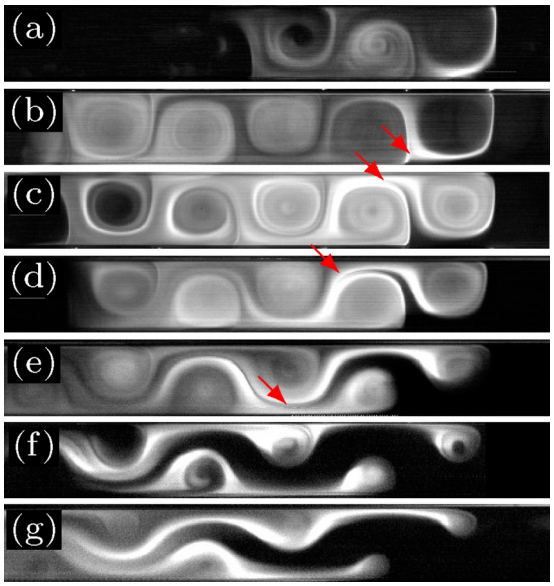

FIG. 5. (Color online) Time-averaged images of steady-state reactions for several wind speeds. $U = 1.4$ mm/s for all. $V_w =$ (a) 0.15 mm/s, (b) 0.16 mm/s, (c) 0.20 mm/s, (d) 0.30 mm/s, (e) 0.60 mm/s, (f) 0.90 mm/s, and (g) 1.2 mm/s. Arrows indicate apparent discontinuities in the frozen front tangent direction.

Above a minimum wind speed, the shape of the frozen front is no longer uniquely determined (modulo the flip-shift symmetry); rather, more than one front shape is possible, depending on the manner in which the front is triggered (Fig. 6). It is possible to trigger a reaction front that pins only to the structure emanating from a single contact point, as in Fig. 6(a). But, the same flow allows for other frozen fronts, such as in Fig. 6(b). The number of different possible frozen front shapes increases with the wind. As can be seen in both Figs. 5 and 6, the front shapes are stretched out significantly with increasing wind speed, spanning more and more vortex cells. For all except the smallest wind speeds, a frozen front can be composed of structures pinned onto adjacent vortex contact points, as in Figs. 5(b)–5(g) and 6(b) and 6(c). For larger wind speeds, additional frozen front shapes are possible. As an example, Fig. 6(d) shows a frozen front composed of two structures originating from contact points separated by five vortex widths.

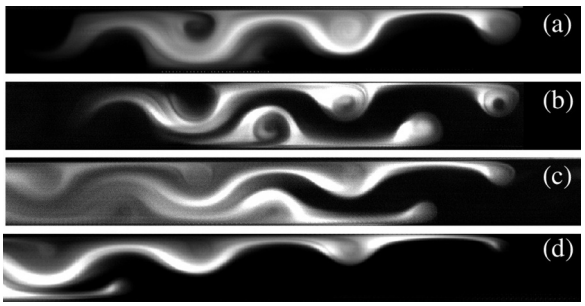

FIG. 6. Multiple frozen fronts are realized with the same flow, depending on how the reaction is triggered. $U = 1.4$ mm/s for all. V_w is 0.90 mm/s for (a), (b) and 1.2 mm/s for (c), (d).

Experimentally, the more complex steady-state front shapes are often found by simultaneously triggering the reaction in multiple locations. However, these complex shapes appear to be sometimes accessible with even a single, well-placed trigger. A more detailed theoretical treatment of these "basins of attraction" is in preparation.

For large enough wind, the stable state is lost completely, with the front being "blown backwards" downwind. A complete parameter space showing the range of wind speeds for frozen fronts can be found in Ref. [10].

III. BIM REVIEW

We model advection-reaction-diffusion systems, such as the above experiments, by considering only the front. This amounts to taking the so-called "sharp-front" or geometric-optics limit. While some other studies have made use of a grid-based computational scheme [23,24], focusing on the front is numerically economical and theoretically insightful. By assuming that the front progresses in a curvature-independent way [31,32], the front may be regarded as the collection of independent front elements that comprise it. Although not crucial to the basic ideas here, we also assume that the "burning speed" [33] (i.e., front propagation speed in the local fluid frame) is homogeneous and isotropic.

A front is the oriented boundary of a burned region with orientation defined by the normal vector $\hat{\mathbf{n}}$ pointing away from the burned region. (We can also refer to the orientation using the tangent vector $\hat{\mathbf{g}}$ where $\hat{\mathbf{n}} \times \hat{\mathbf{g}} = +1$, i.e., pointing out of the plane.) Denoting by $\mathbf{r}$ the xy position of a front element and by θ the angle from the x axis to $\hat{\mathbf{g}}$, a front is a curve in $xy\theta$ space that satisfies the *front-compatibility criterion*

$$\frac{d\mathbf{r}}{d\lambda} \propto \hat{\mathbf{g}}(\theta), \tag{1}$$

where λ is some smooth parametrization of the curve. The above assumptions lead to the following three-dimensional ordinary differential equation (ODE) governing the evolution of an individual front element $(\mathbf{r}(t),\theta(t))$:

$$\dot{\mathbf{r}} = \mathbf{u} + v_0\hat{\mathbf{n}}, \tag{2a}$$

$$\dot{\theta} = -\hat{n}_i u_{i,j}\hat{g}_j, \tag{2b}$$

where $\mathbf{u}$ is the prescribed fluid velocity field, which is nondimensionalized by dividing by U, the maximum fluid vortex speed in the absence of wind. That is, in the absence of wind, the maximum value of u is unity. Here, $v_0 = V_0/U$ is the nondimensionalized front propagation speed in the comoving fluid frame. The position variable $\mathbf{r}$ is scaled so that the width of each vortex and of the channel is unity. Time is scaled by the advection time D/U, where D is the (dimensionful) vortex width. Note that $\hat{\mathbf{g}} = (\cos\theta, \sin\theta)$ and $\hat{\mathbf{n}} = (\sin\theta, -\cos\theta)$ indicate the tangent to the front element and the normal direction (propagation direction), respectively. Furthermore, $u_{i,j} = \partial u_i/\partial r_j$ and repeated indices are summed. The total translational motion of a front element is the vector sum of the fluid velocity and the front propagation velocity in the fluid frame [Eq. (2a)]. The change in orientation is determined entirely kinematically; Eq. (2b) describes the angular velocity of a material line embedded in the fluid. It is also a special case of the Jeffery equation [34] for rotation of an ellipsoidal tracer in a 2D flow in the case where the aspect ratio of the tracer is infinite, i.e., for a thin rod (or a front element in our case). It is worth noting that this three-dimensional (3D) ODE can also be derived from the G equation, widely used in the modeling of combustion [35].

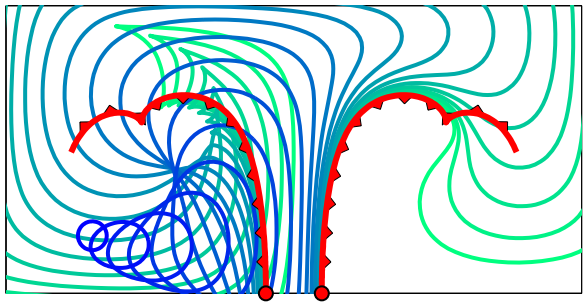

FIG. 7. (Color online) Evolution of reaction front in two counter-rotating vortices. Stimulation (small blue circle) on lower left grows while being acted on by the flow. Two BIMs (red) emanate from burning fixed points on the bottom channel wall. The "burning direction" of each BIM is indicated by red triangles. The reaction passes through oppositely oriented BIM, but is blocked by cooriented BIM. Finally the reaction front wraps around cusp of right BIM.

Invariant manifolds of the full 3D ($xy\theta$) dynamics [Eq. (2)] depend upon both the fluid flow and front propagation, and therefore differ from the invariant manifolds of the underlying advection dynamics. We focus on the 1D unstable manifolds attached to the burning fixed points [fixed points of Eq. (2)] that are of stability type stable-stable-unstable (SSU). We call these burning invariant manifolds (BIMs). It has been demonstrated theoretically and experimentally that these BIMs are "one-way" barriers to front propagation in flows (Fig. 7). That is, they prevent reactions from crossing in one direction but allow them to cross in the other. It is somewhat surprising that these codimension-two manifolds are in fact barriers. BIMs are not generic curves through $xy\theta$ space; they obey the front compatibility criterion 1 [8]. All fronts, including BIMs, obey the front no-passing lemma: no front can overtake another front from behind.

An interesting consequence of the front propagation dynamics is the ability to create cusps in fronts and in the BIMs. In time-independent flows, cusps mark a change in the bounding nature of BIMs. Figure 7 illustrates the evolution of a small circular front (lower left, blue). During its evolution (blue to green), it passes through the left BIM (red) because of their opposite orientation. It then presses up against the right BIM (cooriented) and follows closely until reaching the BIM cusp where the BIM's relative orientation changes, thus allowing passage of the reaction front. We define the *BIM core* as the BIM segment that includes the burning fixed point and extends in both directions until reaching either a cusp, a new burning fixed point, or infinity.

IV. FROZEN FRONTS: BASIC THEORY

Consider a fluid domain D that is connected, but not necessarily simply connected. In this paper, we focus on a channel flow where $D = \mathbb{R} \otimes [0,1]$, but the results obtained

in this section are general. We now introduce a more precise mathematical definition of frozen front than the more intuitive definition used thus far. First, we define *frozen domain* as a burned subdomain of D that is invariant under the burning dynamics and stable to perturbation [36]. (See Appendix B for a precise discussion of this notion of stability.) Since the fluid is incompressible, neither the frozen domain nor its complement may be of finite area. A *frozen front* is the oriented boundary of a frozen domain that separates the burned from the unburned fluid. (The frozen domain boundary that coincides with the boundary of D, i.e., a domain wall, is then not considered part of the frozen front.) As with any front, we choose the orientation of the frozen front to be a unit vector normal to the frozen front pointing outward from the burned region. Since the frozen domain is unbounded, the frozen front cannot be a closed curve. Note that a frozen domain does not correspond to a comoving parcel of fluid, but is a set of locations in the laboratory frame. Similarly, a frozen front is not a material line (nor is any front with nonzero v_0).

Consider a particular frozen front F as a curve in $xy\theta$ space. An individual front element on F can evolve into the interior of the frozen domain, but not vice versa. Since the frozen domain is invariant, the time evolution of F under Eq. (2) includes F for any time t. In other words, the backward trajectory of any point on F remains on F. Thus, the frozen front must be the union of segments of front element trajectories, and is hence a piecewise smooth curve. Each segment follows a trajectory from $t = -\infty$ to some $t = t_f$. This implies each segment lies within the unstable manifold emanating from a fixed point, which may be at infinity.

On a smooth segment of frozen front a front element is either a fixed point of the flow, or it "slides" along the segment satisfying $\dot{\mathbf{r}} \propto \hat{\mathbf{g}}$. Any frozen front can thus be decomposed into a collection of these *sliding fronts* (Appendix A). Here, we summarize the geometry of sliding fronts detailed in Appendix A. First, sliding fronts only exist in the domain where $|\mathbf{u}| \geqslant v_0$. We refer to this domain as the fast zone and the complementary domain as the slow zone. In the fast zone, the structure of the sliding fronts can be simply characterized. At every point in the fast zone interior, there are two allowed sliding front orientations characterized by the angle

$$\beta = \arccos(-v_0/|\mathbf{u}|) \tag{3}$$

between the front propagation direction $\hat{\mathbf{n}}$ and the fluid flow $\mathbf{u}$ (Fig. 8, Lemma 8). In the limit $v_0/|\mathbf{u}| \to 0$, the two sliding fronts become parallel (burning in opposite directions) and align with the streamlines, thus recovering the advective case. We refer to these two choices of orientation as "+" and "−" corresponding to $\mathrm{sgn}(\dot{\mathbf{r}} \cdot \hat{\mathbf{g}})$. Each choice of orientation defines a set of sliding fronts whose projection foliates the fast zone. When the sliding fronts are considered as curves in $xy\theta$ space, they foliate a two-dimensional surface which is a double-branched covering of the fast zone (see Figs. 22 and 23 for examples).

Consider a burned region bounded by two sliding fronts (on different branches) that meet at a point as in Fig. 8. In principle, the burned region may be either locally concave or locally convex at this point. However, the convex case is not relevant to frozen fronts because any convex corner will be smoothed out after an arbitrarily short evolution. Therefore,

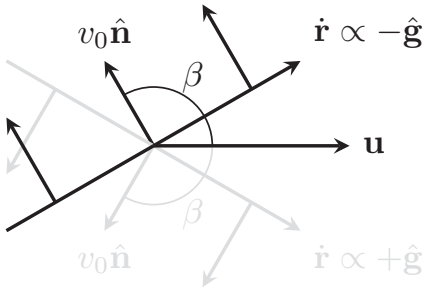

FIG. 8. A generic intersection of two sliding fronts (one black, one gray). Each sliding front's propagation vector $v_0\hat{\mathbf{n}}$ cancels the normal component of the fluid velocity $\mathbf{u}$, leaving only motion tangent to the front. The two orientations (black and gray) are symmetric about $\mathbf{u}$.

in the interior of the fast zone, a frozen front is simply a union of smooth curves that meet at concave angles specified by the local burning-to-fluid-speed ratio $v_0/|\mathbf{u}|$. In the limit $|\mathbf{u}| \to {}^+v_0$, the two branches meet on the boundary of the slow zone. At all such points of the boundary, two sliding fronts meet with burning directions $\hat{\mathbf{n}}$ aligned. There are two cases to consider.

In the first case, assume $\hat{\mathbf{n}}$ is not perpendicular to the slow zone. Then, the sliding front trajectory passes through the fold joining the two branches in such a way that it forms a cusp in the xy plane (Fig. 9). We observed above that cusps mark a change in the bounding behavior of BIMs. This change occurs at cusps along any sliding front (including BIMs), which implies that *a frozen front cannot contain a cusp*. Figure 10 illustrates why; it shows the two possible burned regions that would be bounded by such a cusp. In both cases, one segment of the sliding front has a burning direction incompatible with, i.e., pointing into, the proposed burned region.

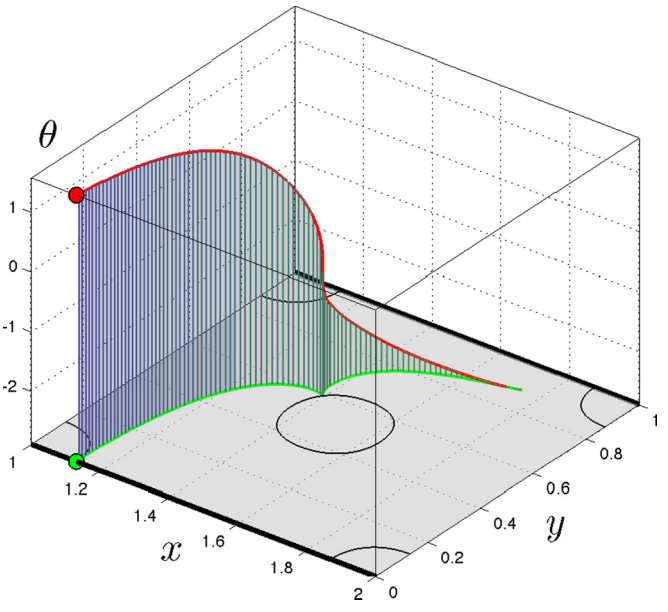

FIG. 9. (Color online) The BIM (red) is a smooth curve in $xy\theta$ space. Its projection (green) onto the xy plane has a cusp on the boundary of the slow zone.

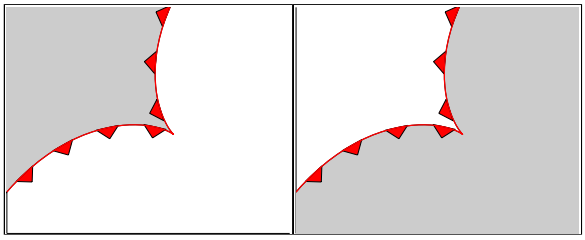

FIG. 10. (Color online) A sliding front (red) with a cusp cannot bound a burned region (gray). Either choice of shading leads to an incompatibility in front orientation in which one piece of the front points into the burned region.

Referring to Fig. 11, as $\hat{\mathbf{n}}$ becomes perpendicular to the slow zone at the point **x**, the cusp becomes tangent to the slow zone. By symmetry, a cusp also approaches **x** from the other side.

In the second case, where $\hat{\mathbf{n}}$ is perpendicular to the slow zone, Ref. [8] showed that the sliding front must meet the slow zone at a burning fixed point **x**. This could be thought of as the meeting of two cusps (Fig. 11). Each segment of the cusp on the left pairs with its symmetric segment on the right to form a smooth curve in xy space passing through **x**. Each of these two combined curves is a 1D stable or unstable manifold of **x**. There are four possible stability types of burning fixed points in $xy\theta$ space: SSS, SSU, SUU, and UUU. These are illustrated in Fig. 24. For SSU and SUU burning fixed points, the dynamics restricted to the sliding surface is of stability SU (Lemma 1). Figure 24 illustrates the 1D stable and unstable manifolds attached to such burning fixed points. For SSS and UUU points, the dynamics within the constraint surface is of stability SS and UU respectively (Lemma 1). Since the burning fixed point is either a sink or source in this case, it is met by an infinite number of sliding trajectories.

Only two of the four stability types can occur on a frozen front. Suppose a frozen front is tangent to a slow zone at a burning fixed point where the burning direction is into the slow zone, as for SUU or UUU stability types. Although the burned region behind the burning fixed point does not intersect the slow zone, a small perturbation of the burned region at the burning fixed point can intersect the slow zone.

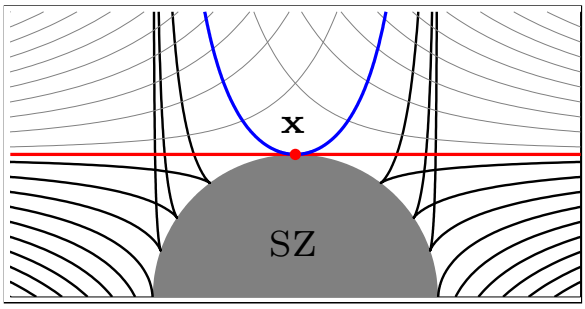

FIG. 11. (Color online) Sliding fronts (black) strike the slow zone, forming cusps on either side of an SSU burning fixed point **x**. As the cusps on either side approach **x**, they become more horizontal, eventually joining tangent to each other at **x**. Here they are stable (blue parabolic) and unstable (red horizontal) invariant manifolds of **x** (and still sliding fronts).

Once any of the slow zone is burned, the entirety of the slow zone must eventually be burned and remain burned forever (Lemma 2). Since we require frozen fronts to be stable under small perturbations (Appendix B), SUU and UUU burning fixed points cannot occur on a frozen front.

The two remaining stability types SSU and SSS can exist on a frozen front. We previously showed that the frozen front consists of unstable manifolds. Only the SSU points have unstable manifolds. Finally, since cusps are not allowed on frozen fronts (shown earlier), we have one of the main results of this paper.

Proposition 1. Frozen fronts are built from BIM cores. More precisely, each frozen front is generated by some set $\mathcal{S}_{\text{frozen front}}$ of SSU burning fixed points. The frozen front is obtained by tracing the unstable manifold from each point in $\mathcal{S}_{\text{frozen front}}$ until one of three things occurs: it intersects any other BIM core emanating from $\mathcal{S}_{\text{frozen front}}$; it intersects any domain boundary; or it terminates at an SSS burning fixed point.

So far we have focused our attention on the generation of the frozen front from burning fixed points. Here, we shift our attention to consider how the sliding segments of a frozen front end. We have already discussed the most common case where segments intersect at a concave corner. There exist two other possibilities: termination on an SSU or SSS burning fixed point.

An SSU burning fixed point has a stable manifold that contains an *incoming* sliding front. A frozen front can therefore contain a segment which is a heteroclinic connection consisting of a sliding front between SSU points. Figure 12(b) shows two SSU burning fixed points joined by such a connection flowing from the upper to the lower burning fixed point. This configuration is a frozen front; in particular, it is stable to perturbations of the burned region (Appendix B). In one sense, the frozen front is also structurally stable because generic perturbations of the flow yield frozen domains with a similar shape [Figs. 12(a) and 12(c)]. In another sense, it is not structurally stable because generic perturbations break the heteroclinic connection, thus altering the dynamics along

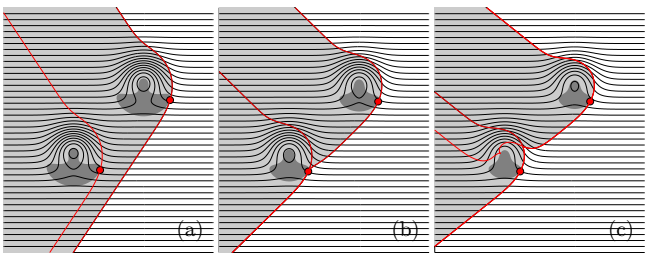

FIG. 12. (Color online) The SSU-SSU connection is not structurally stable as the wind speed is varied. Nevertheless, the frozen domain (light gray) varies continuously. Slow zones are dark gray. (a) The relation $v_w < v_c$ places the lower SSU point behind the frozen front attached to the upper SSU point. (b) The equality $v_w = v_c$ makes the unstable manifold from the upper SSU point coincide with the stable manifold of the lower point. (c) The relation $v_w > v_c$ pushes the lower SSU point ahead, placing it and its BIM on the frozen front. The frozen front is now composed of two BIMs meeting at a concave corner.

the front. Some of these perturbations cause the lower SSU burning fixed point to fall behind the frozen front [Fig. 12(a)], while other perturbations cause it to push through, and in doing so contribute a segment of unstable sliding front to the frozen front [Fig. 12(c)]. As seen in Figs. 12(b) and 12(c), both of these perturbations return the system to the generic case. So, while SSU burning fixed points can exist as "termination points" along a frozen front, this is not generic.

Finally, we consider the SSU to SSS connection. The SSS point attracts all points within a 3D neighborhood and, therefore, it attracts all sliding fronts within some neighborhood on the invariant sliding surface. It might then seem that this SSS point can be on a frozen front containing any of these incoming sliding fronts. However, the sliding front must reach the SSS point without having formed a cusp. This can only happen if the eigenvalues of the SSS point are real. Such SSS points do exist, albeit for what appears to be a small parameter range.

V. THEORY: WINDY ALTERNATING VORTEX CHAIN FLOW

We continue our discussion of frozen fronts using a simple numerical model of the experimental fluid flow.

A. Numerical model

The stream function that describes the flow is

$$\Psi = \frac{1}{\pi}\sin(\pi x)\sin(\pi y) - v_w y, \tag{4}$$

where $u_x = d\Psi/dy$ and $u_y = -d\Psi/dx$. This model has been used in several previous studies, on both fluid mixing and reacting flows, yielding reasonable agreement with experiment. Our intent here is to illustrate the theory of frozen fronts for a particular fluid flow, and to reproduce basic features of the experimental flow in Sec. II.

There is a weak three-dimensional component to the vortex flow due to Ekman pumping that carries fluid toward the vortex centers at the bottom of the fluid layer and up through the vortex cores [37]. This effect is not included in the model. Also, while the model has free-slip boundary conditions, this is certainly not true in the experiment. Nevertheless, the simplified free-slip model of Eq. (4) has been used successfully in modeling several experiments on passive transport and front propagation in vortex flows [14,20,22,24,25]. The last term in Eq. (4) numerically models the fluid wind observed in the moving frame of the vortices.

B. Dynamical systems analysis

We begin by considering a flow where the wind is of insufficient strength to produce a frozen front [Fig. 13(a)]. The streamlines indicate that this is essentially a vortex flow, but with a sinuous, left-moving jet. In Fig. 13(b), a small circular stimulation (purple) is made in the lower left. This circle evolves (purple to red) outward to the left and right while being deformed by the flow. The rightward-moving front is able to make slow progress "upwind." Notice though that it is blocked at the vortex boundary near the bottom and middle, and must wind around through the top of the channel. In this way, the reaction continues winding rightward through the channel indefinitely [Fig. 13(c)].

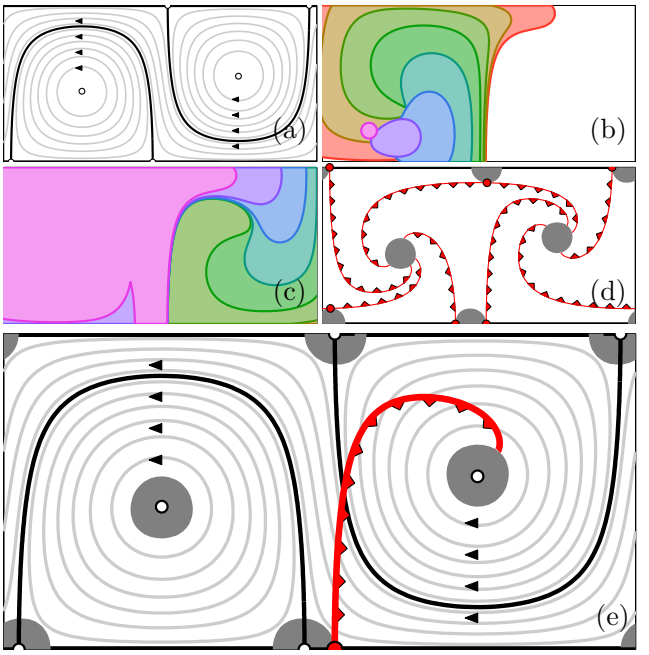

FIG. 13. (Color online) Small wind speed ($v_0 = 0.3$, $v_w = 0.15$). (a) Fluid flow streamlines, fixed points, and attached invariant manifolds. (b) Sequence of fronts (small purple circle to red indicates temporal evolution) shows preliminary convergence near bottom to roughly vertical curve. (c) Further evolution; lower edge converges to curved line while the rest proceeds around and to the right. (d) BIMs attached to burning fixed points. Slow zones shaded gray. (e) The one BIM most important for above front evolution, shown against advective structure.

Figure 13(d) illustrates all slow zones (gray), SSU burning fixed points (red), and BIMs (red with arrows indicating the burning direction) in this system. Two of the slow zones contain the elliptic advective fixed points in the vortex centers. The others contain hyperbolic advective fixed points on the channel walls. Note that the slow zones are slightly offset from a square lattice. This is due to the small wind added. We show only the SSU burning fixed points since, as shown in (Proposition 1), they are the generators of the unstable manifolds which combine to form frozen fronts. Each burning fixed point lies on a slow zone boundary and, because it is SSU, is oriented away from the slow zone. The BIMs emanating from these burning fixed points are similarly oriented. Each BIM spirals into a vortex center where it forms a cusp on an elliptic slow zone (i.e., a slow zone that contains an elliptic advective fixed point). Only the incoming portion of the cusp is pictured because, as shown earlier, the frozen front cannot contain cusps, and so the remainder of the BIM will not be relevant.

Figure 13(e) summarizes the dynamical structures relevant to the behavior observed in Figs. 13(b) and 13(c). The BIM core shown is responsible for blocking front propagation at the bottom and center of the channel in Fig. 13(b). The transverse stability of the BIM leads to the front's rapid convergence upon it [Fig. 13(b)]. As the front evolves further [Fig. 13(c)],

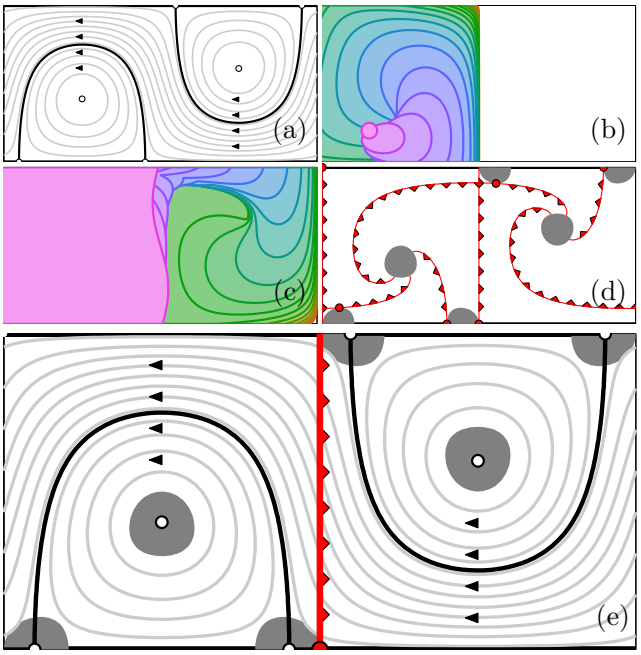

FIG. 14. (Color online) Critical wind speed ($v_0 = v_w = 0.3$). (a) Advective structure; similar to previous case. (b) This time, front progress (from the left) is completely blocked. (c) Perturbation of burned region shows instability, therefore not a frozen domain. (d) Several BIMs, burning fixed points, and slow zones. (e) BIM of interest is a straight vertical line, coincides with separatrix of nonwindy flow.

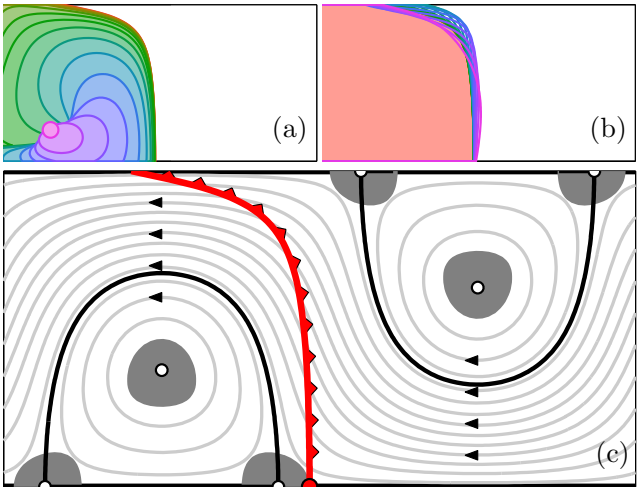

FIG. 15. (Color online) Wind greater than critical ($v_0 = 0.3$, $v_w = 0.4$). A stimulation on the left (a) converges onto a smooth curve that spans the channel. In (b) a sinusoidal perturbation of this curve converges back to the curve, implying that it is stable. (Only the last front is filled.) (c) The BIM responsible for the frozen front spans the channel with no cusps.

it reaches the cusp at the end of the BIM core and winds around it. The BIM core does not form a complete span across the channel, and thus does not form a *global* barrier to the propagation of fronts. This is the situation seen in experimental images Figs. 4(a)–4(c).

Now, we increase the wind speed until it precisely balances the burning speed $v_w = v_0$ (Fig. 14). Stimulating in the lower left (purple) we find that the reaction approaches a vertical curve [Fig. 14(b)], and so the reaction is confined to the left side. This appears to be a candidate for a frozen domain. In Fig. 14(c), we test the stability of this region by introducing a small sinusoidal perturbation. The rightward component of this perturbation grows, eventually filling in the entire cell to the right, demonstrating that this region is not stable and therefore not a frozen domain.

Let us examine the dynamical structures in Figs. 14(d) and 14(e). The increase in wind has caused the slow zones to shift slightly relative to Figs. 13(d) and 13(e); the two on the lower boundary move together, as do the two on the upper boundary; those in the vortices move up or down depending on their rotational sense. The central BIM is now a straight vertical line. It is important to note that this BIM spans the entire channel with no cusp, thus creating a *global* barrier to front propagation. Symmetry of the flow indicates that this BIM terminates at an SUU burning fixed point at the top of the channel. We have previously argued that such a fixed point could not be on a frozen front, and it is this fixed point that leads to the instability demonstrated in Fig. 14(c).

Now, we increase the wind beyond the critical value. In Fig. 15(a), a stimulation on the left converges to a burned region bounded by a smooth curve spanning the channel. Unlike in Fig. 14(c), a small rightward perturbation in Fig. 15(b) converges back to this smooth curve, and hence this curve is a frozen front. Figure 15(c) shows that the smooth bounding curve is the BIM emanating from the bottom burning fixed point. Note that this BIM terminates at a point on the boundary that is not a burning fixed point. This explains the situation seen in experimental images Figs. 4(d)–4(f) as well as Fig. 5(a). Also note that this change is not accompanied by a change in the fluid flow topology.

Now that we have seen BIMs act as both local and global barriers, we would like to understand the transition between these two cases in more detail. Imagine a deformation that takes the BIM in Fig. 13(e) to the BIM in Fig. 15(c): What might this deformation look like? Lemma 8 ensures that the angle between BIMs and streamlines is nonzero throughout the interior of the fast zone. Therefore, a BIM cannot form a tangency with the channel wall (which must coincide with a streamline) in the interior of the fast zone. Note, however, that a BIM *cusp*, on the boundary of a slow zone, may encounter the channel wall without forming a tangency. In fact, this occurs when the cusp is perpendicular to the channel wall (Lemma 7). This observation suggests two deformation strategies: either move the existing cusp on the elliptic slow zone to the wall, or create a new cusp on the hyperbolic slow zone and slide the cusp to the wall. While the first mechanism seems more straightforward, and has not been ruled out theoretically, it has not yet been observed. However, the second mechanism is observed here.

In Fig. 16, we increase v_w through the critical value $v_w = v_0$ and follow the transformation of the BIM. Beginning with a subcritical v_w value in Fig. 16(a), we see the BIM (green) that comes up from burning fixed point A (not shown) on the bottom wall and veers off to the right to form a cusp on the

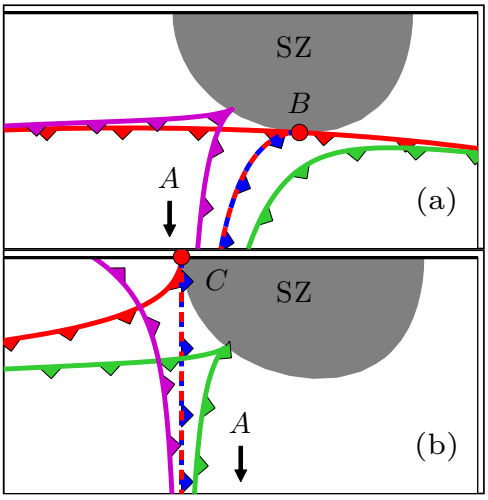

FIG. 16. (Color online) The basic mechanism in the transition to the first frozen front. We increase the wind speed, showing the interplay between the BIM from burning fixed point A (not shown) and the upper slow zone and its burning fixed points. (a) An SSU burning fixed point B lies on the bottom of the slow zone. Attached to it are BIMs (red) going left and right, both of which end in cusps on elliptic slow zones (not shown). (i) A BIM (green) comes up from the SSU burning fixed point A below (not shown) and then shadows the unstable BIM (red) going to the right. (ii) The BIM (red and blue dashed) forms a tangency, i.e. a heteroclinic connection, with the burning fixed point B. (iii) The BIM (purple) is blown left, behind the heteroclinic connection, forming a cusp. (b) An SUU burning fixed point C is shown at the top of the channel. A BIM (red) lies within its unstable manifold and goes off to the left. (iv) A BIM (green) slides leftward along the slow zone, approaching the burning fixed point C. (v) The BIM (red and blue dashed) forms a second heteroclinic tangency with burning fixed point C. (vi) The BIM (purple) is blown left, beyond this heteroclinic connection, forming a complete span across the channel. Since the burning fixed point positions and slow zones change slightly with v_w, the specific burning fixed points B and C shown, as well as their slow zones, are calculated for the parameter values of the heteroclinic connections.

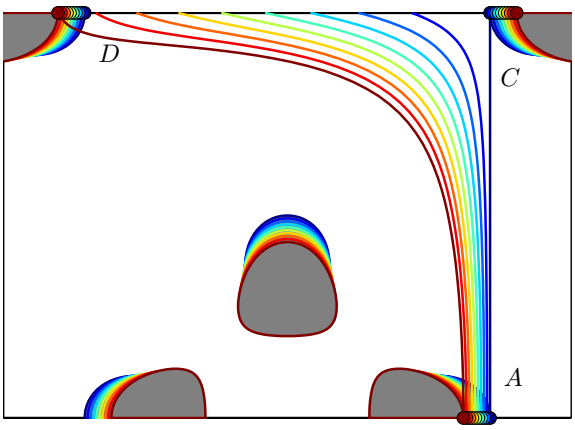

FIG. 17. (Color online) A series of frozen fronts for increasing wind values ($v_0 = 0.3$, $v_0 < v_w < 1.7v_0$, blue vertical to red curve). The BIM attached to burning fixed point A is swept backward until it intersects burning fixed point D The slow zones also shift and are colored accordingly. Compare to front shapes in experimental images.

elliptic slow zone (not shown). This cusp marks the end of the BIM core.

Increasing the wind, the BIM is "blown backward" developing a tangency (red and blue dashed) with the upper slow zone. This tangency is not forbidden because the slow zone is not defined by a streamline. Since the front is burning away from the slow zone, the tangency must occur at either an SSU or SSS burning fixed point on the upper slow zone (according to Lemma 6 and Fig. 24). Because the slow zone is convex in this case, the burning fixed point must be SSU. The heteroclinic connection is illustrated by the coincidence of the unstable BIM of burning fixed point A and the stable BIM of burning fixed point B (red and blue dashed).

Continuing to increase the wind, the BIM is blown further backward. Now, it does not meet the slow zone at a tangency, and so the heteroclinic connection is broken, giving way to a cusp; the other option allowed by Lemma 6. This cusp slides along the slow zone, with its angle changing to remain perpendicular to the fluid flow (Lemma 6). The cusp must rotate counterclockwise, at least initially, so that its tangent points into the slow zone, as rotating clockwise would require the BIM to enter the slow zone.

The BIM soon arrives at another tangency with the slow zone [Fig. 16(b)]. Here, however, the BIM is burning into, rather than away from, the slow zone. This tangency implies a heteroclinic connection with the SUU burning fixed point C. (Again, the UUU case cannot occur because the slow zone is convex; see Fig. 24.) In a generic three-dimensional dynamical system, heteroclinic connections between SSU and SUU fixed points are codimension-two occurrences. In this system, however, the BIMs are constrained to the two-dimensional sliding surface, and so the heteroclinic connection is a codimension-one occurrence. Said loosely, if a BIM is to sweep from one side of a slow zone to the other, the BIM cannot avoid connecting with at least two burning fixed points on the slow zone boundary.

Increasing the wind still further, the BIM, blown entirely clear of the slow zone, spans the entire channel, uninterrupted by cusps. We have now arrived at the frozen front configuration in Fig. 15(c). This frozen front topology persists for a significant range of wind values. As seen in Fig. 17, the shape of this front can be nearly straight, or more boomerang shaped, depending on the applied wind. Note that it is only due to the symmetry of the flow that the second heteroclinic connection in Fig. 16(b) occurs exactly when the BIM core first spans the channel.

At approximately wind value $v_w = 0.34 = 1.7v_0$, the BIM encounters the upper left slow zone in Fig. 17. Just like the BIM transition in Fig. 16, we must form a heteroclinic tangency (Lemma 6 and Fig. 24) to a new SSU burning fixed point denoted burning fixed point D. (Note the latter is rotated by roughly $\pi/2$ CCW in comparison to Fig. 16.) Foretelling this tangency, the red curves in Fig. 17 begin to curve upward near the upper channel wall. Once again, symmetry of the flow requires that burning fixed point D be on the upper channel wall.

As v_0 is increased still further, the BIM forms a cusp just behind the unstable BIM attached to burning fixed point D

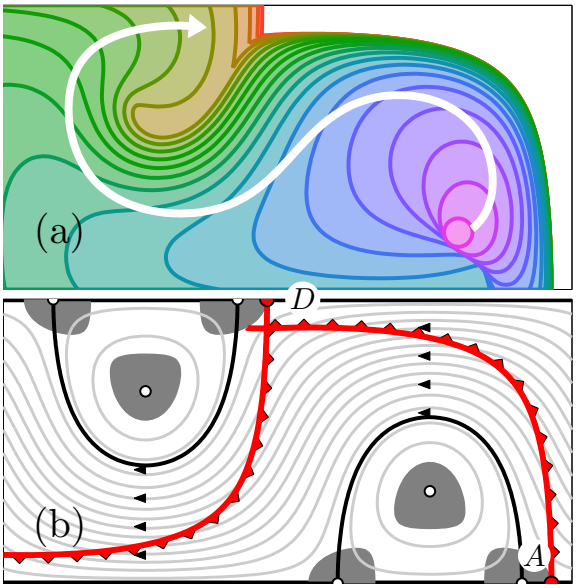

FIG. 18. (Color online) A composite frozen front formed from two BIMs, neither one a frozen front ($v_0 = 0.3$, $v_w = 0.525$). The evolving front rapidly converges to BIM A and then winds around its cusp. However, it is prevented from going further rightward by the short segment of BIM D.

[Fig. 18(b)], as seen in the mechanism in Fig. 16(a). Note that while a front may wrap around the newly formed cusp attempting to bypass the initial BIM, it will shortly encounter the BIM attached to burning fixed point D which has closed off this pathway [Fig. 18(a)]. Here, we have a frozen front that is composed of two distinct BIMs. Note that the burning region has a concave corner, with opening angle given by Lemma 8. The appearance of this concave corner is exactly what was observed in the experimental frozen front [Fig. 5(b)].

The sequence in Fig. 19(a) takes the BIM through a series of encounters with slow zones as the wind speed is increased. (Here, we consider $v_0 = 0.2$ for simplicity.) The first encounter is the attachment and detachment mechanism with the upper right slow zone, analogous to that in Fig. 16. Here, however, the BIM detachment does not result in a BIM core that spans the channel. Rather, the BIM continues for some distance and then spirals in toward the elliptic slow zone in the upper left, where it forms a cusp. As the wind speed increases, the cusp slides clockwise around the slow zone until the BIM forms a new tangency with the upper left slow zone. The cusp on the elliptic slow zone is "cut off" by this tangency, which dynamically precedes it along the BIM. This begins the mechanism of Fig. 16 again, after which the BIM core forms a complete span and defines a frozen front.

Figure 19(b) shows a similar sequence as Fig. 19(a) for $v_0 = 0.3$. The main difference between these two images is that three slow zones have merged into one in Fig. 19(b). Consequently, the initial detachment of the BIM from the upper right of the slow zone results in a new cusp formed near the bottom of the same slow zone. Furthermore, as the cusp moves clockwise around the slow zone, it is never "cut off," but instead slides along the slow zone to the channel wall.

By flip-shift symmetry of the flow, the BIM attached to burning fixed point D has undergone the same transition as

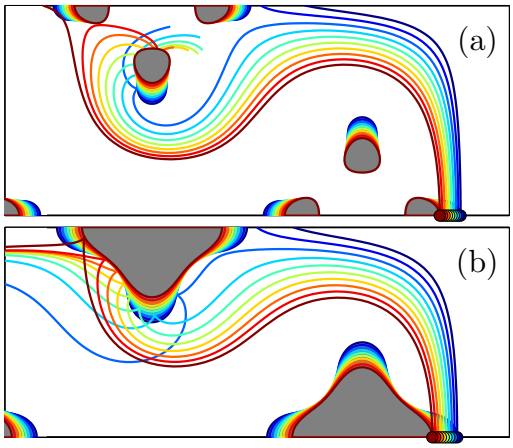

FIG. 19. (Color online) Increasing the wind beyond first instance of frozen front generates new transitions. (a) ($v_0 = 0.2$, $0.3 < v_w < 0.6$) Blue (rightmost) frozen front rapidly attaches to and detaches from slow zone. Upon detaching, the BIM "jumps" straight to a cusp on an elliptic slow zone. With even higher wind, another attachment and detachment leads again to a complete span. (b) ($v_0 = 0.3$, $0.45 < v_w < 0.8$) Illustration of similar transitions where "jumping" occurs all within a single connected slow zone.

the BIM attached to burning fixed point A and so forms a frozen front as well [Fig. 20(a)]. Importantly these two frozen fronts intersect. Consequently, in addition to the frozen domains defined by single BIMs, the *union* of two neighboring frozen domains defines a distinct frozen domain. This union is continuously related to the frozen domain observed in Fig. 18(a) as v_w is increased. In Figs. 15 and 18, there is

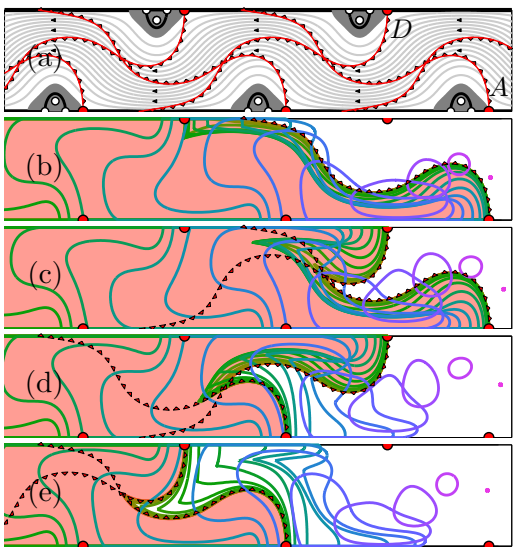

FIG. 20. (Color online) Frozen front diversity and sensitivity to initial stimulation ($v_0 = 0.3$, $v_w = 0.95$). (a) BIMs A and D (related by flip-shift symmetry) each form a complete span, and intersect. Nearby stimulations (small pink dots near the right side) lead to different asymptotic frozen domains. The frozen domains fall into two classes: (b) and (c)–(e). (b) The frozen front is composed of a single BIM, which spans the channel. (c)–(e) The frozen front is composed of two BIMs.

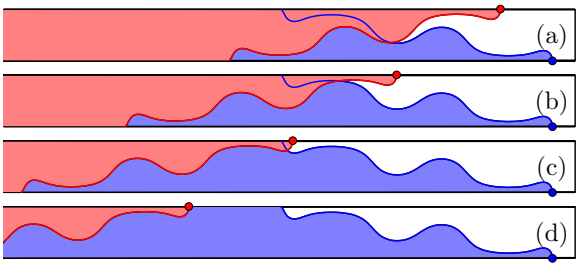

FIG. 21. (Color online) For the windy alternating vortex chain flow we can enumerate the increasing number of possible frozen domains that occur with increasing wind speed. In this example, there are four frozen front shapes (up to flip-shift symmetry) ($v_0 = 0.2$, $v_w = 1.18$).

a one-to-one correspondence between frozen domains and vortices in the channel. Now, in Fig. 20, the diversity of frozen domains (at fixed v_0 and v_w) has increased. We can have either a frozen front formed by a single BIM core [Fig. 20(b)] or by two intersecting BIM cores [Figs. 20(c)–20(e)]. Note that the diversity of frozen fronts in Figs. 20(b)–20(e) is produced by small changes to the initial stimulation point.

As the wind is increased, the process in Fig. 19 is repeated. The BIM slides along the upper channel wall until it encounters an SSU burning fixed point on a slow zone. It moves around the slow zone until it moves completely to the left of the slow zone and reconnects to the channel wall. This process occurs once for each vortex pair. After each such occurrence, the BIM acquires a new intersection with another BIM emanating from the opposite side of the channel. We can thereby enumerate all frozen domains of this system for given values of v_0 and v_w (Fig. 21). Finally, when $\min(|\mathbf{u}|) > v_0$, there are no slow zones, and therefore no burning fixed points, and therefore no frozen fronts.

VI. CONCLUSIONS

The ability of a heterogeneous flow to freeze reaction fronts in the presence of an imposed wind appears to be quite general. Frozen fronts ("sustained patterns") have been observed numerically in simulations of oceanic plankton blooms [38]. Frozen fronts have also been seen both experimentally and numerically in reacting flows in a porous media with a throughflow [39,40]. We have also conducted experiments on frozen fronts in extended flows composed of two-dimensional arrays of vortices, either ordered or disordered [41]. As is the case in this paper, the frozen fronts in an extended flow with a wind are due to patterns of overlapping BIMs.

This work suggests several directions of future research. In the context of design and control, this analysis could be used to develop a reacting fluid flow with some desired property. An obvious example is a system with maximal reaction rate. Given some class of accessible fluid flows, the reaction rate can be readily maximized by computing the lengths of frozen fronts. Another example is reaction rate stability. We might be given a particular flow perturbation and seek the base flow that minimizes reaction rate fluctuation.

It may be desirable to generate a frozen front with a particular geometry. For instance, there may be a region in the neighborhood of the frozen front that we wish to keep strictly separated from the front (e.g., a sensor in the vicinity of a combustion front that cannot withstand the temperatures of the front itself). The analysis here provides a detailed connection between the stream function and frozen front shape making these questions accessible.

ACKNOWLEDGMENTS

This work was supported by the U. S. National Science Foundation under Grants No. PHY-0748828 and No. CMMI-1201236 (K.A.M.) and Grants No. DMR-1004744, No. DMR-1361881, and No. PHY-1156964 (T.S.).

APPENDIX A: SLIDING FRONTS

Although we study fronts propagating in time-independent fluid flows, the fronts themselves certainly need not be time invariant. For instance, a fast-propagating front in a weak flow will evolve approximately as a circle of increasing radius. Loosely speaking, this is because each front element in the circle "burns beyond itself." For a front to be time invariant, each element must instead "slide along itself." In this section, we make this statement clear and derive several consequences.

Definition 1. A front element, i.e., a point in $xy\theta$ space, is said to be *sliding* when $\dot{\mathbf{r}} \propto \hat{\mathbf{g}}$, where $\hat{\mathbf{g}} = [\cos\theta, \sin\theta]$. Equivalently,

$$\dot{\mathbf{r}} \cdot \hat{\mathbf{n}} = 0, \tag{A1}$$

where $\hat{\mathbf{n}} = [\sin\theta, -\cos\theta]$.

While the sliding property is defined for any fluid flow, it is of most use when the flow is time independent, as we have assumed throughout this paper and its appendices.

The "sliding" constraint (A1) is illustrated geometrically in Fig. 8. For a given xy location, there are either zero, one, or two solutions for θ satisfying this constraint. Where the fluid speed is small ($|\mathbf{u}| < v_0$), there is no solution; we call such a region a "slow zone."

Lemma 1. There are no sliding elements inside a slow zone.

Proof. Combining the sliding constraint (A1) with Eq. (2), we find $|\mathbf{u} \cdot \hat{\mathbf{n}}| = |v_0|$. This cannot be satisfied for $|\mathbf{u}| < v_0$. ■

Where the fluid speed is large ($|\mathbf{u}| > v_0$), there are two solutions to Eq. (A1). Where the fluid speed equals the burning speed ($|\mathbf{u}| = v_0$), these two solutions are degenerate. We call a region where $|\mathbf{u}| \geqslant v_0$ a "fast zone." The sliding constraint (A1) defines a two-dimensional submanifold of $xy\theta$ space, called the *sliding surface*, which can be viewed as a double-branched surface over the fast zone. Figures 22(a) and 23(a) show the sliding surface for a hyperbolic and an elliptic flow, respectively [42]. In Figs. 22(a) and 23(a), we see that, when viewed from above, these sliding surfaces have a hole in the middle exactly where the slow zone is.

Lemma 2. If at any time some portion of a slow zone is burned, the asymptotic burned domain will include that entire slow zone.

Proof. Within the slow zone, the velocity of the front is everywhere greater than the fluid. Therefore, no direction of motion is forbidden to the front, and so the front will eventually access all parts of the slow zone. ■

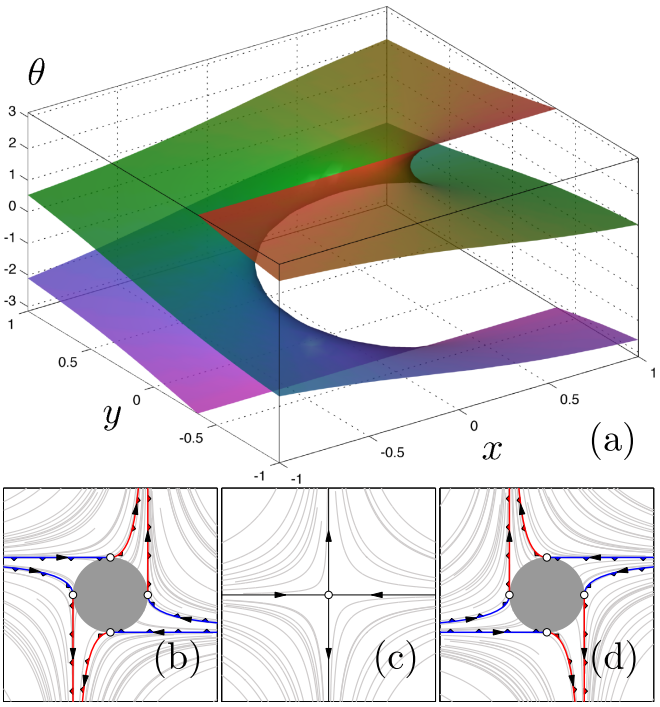

FIG. 22. (Color online) Hyperbolic fluid flow. $\dot{\mathbf{x}} = -A\mathbf{x}$, $\dot{\mathbf{y}} = +A\mathbf{y}$. ($v_0 = 0.35$, $A = 1$) (a) Sliding surface. (b) Streamlines of the $\mathbf{w}_+$ field. (c) Streamlines of the advective fluid flow. (d) Streamlines of the $\mathbf{w}_-$ field.

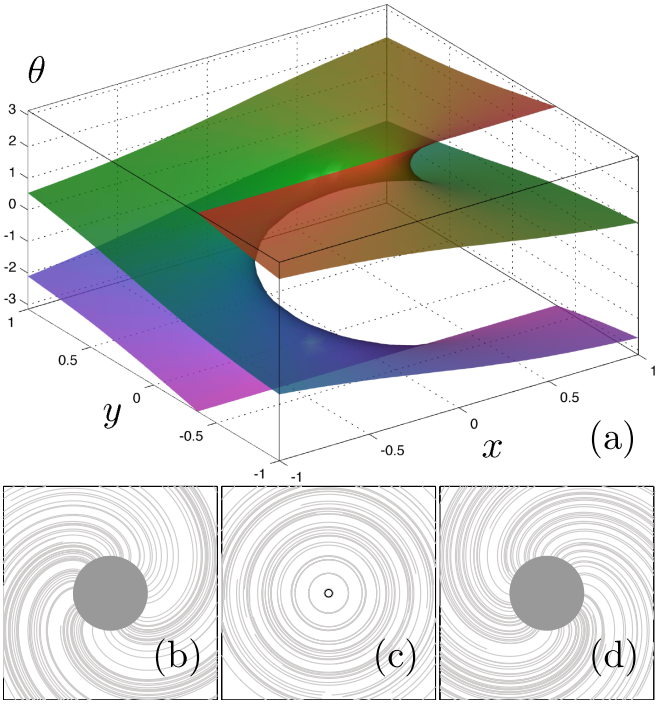

FIG. 23. (Color online) Elliptic fluid flow. $\dot{\mathbf{x}} = -A\mathbf{y}$, $\dot{\mathbf{y}} = +A\mathbf{x}$. ($v_0 = 0.35$, $A = 1$) (a) Sliding surface. (b) Streamlines of the $\mathbf{w}_+$ field. (c) Streamlines of the advective fluid flow. (d) Streamlines of the $\mathbf{w}_-$ field.

Lemma 3. Sliding is an invariant property. That is, if a front element is sliding, every element along its trajectory under Eq. (2) is also sliding. Hence, we may speak of *sliding trajectories*.

Proof. We examine the time derivative of Eq. (A1):

$$\begin{aligned}\frac{d}{dt}(\dot{\mathbf{r}}\cdot\hat{\mathbf{n}}) &= (u_{i,j}\dot{r}_j + v_0\dot{\theta}\hat{g}_i)\hat{n}_i + \dot{r}_k\hat{g}_k\dot{\theta}\\ &= \hat{n}_i u_{i,j}\dot{r}_j + \dot{r}_k\hat{g}_k\dot{\theta}\\ &= \pm|\dot{\mathbf{r}}|\hat{n}_i u_{i,j}\hat{g}_j \pm |\dot{\mathbf{r}}|\hat{g}_k\hat{g}_k\dot{\theta}\\ &= \pm|\dot{\mathbf{r}}|(-\dot{\theta}) \pm |\dot{\mathbf{r}}|\dot{\theta} = 0,\end{aligned}$$

where the first equality follows from Eq. (2a) and the fact that $d\hat{\mathbf{n}}/dt = \hat{\mathbf{g}}\dot{\theta}$, the second from the orthogonality of $\hat{\mathbf{n}}$ and $\hat{\mathbf{g}}$, the third from the sliding assumption $\dot{\mathbf{r}} = \pm|\dot{\mathbf{r}}|\hat{\mathbf{g}}$, and the fourth from Eq. (2b). ■

A consequence of this lemma is that the sliding surface is dynamically invariant. Recall that a front is a curve $(\mathbf{r}(\lambda),\theta(\lambda))$ that everywhere satisfies the front compatibility criterion (1), which is expressed equivalently as

$$d\mathbf{r}/d\lambda\cdot\hat{\mathbf{n}} = 0. \tag{A2}$$

Lemma 4. A trajectory of Eq. (2) is sliding if and only if the curve it sweeps out is a front.

Proof. Choosing $\lambda = t$, Eq. (A1) is equivalent to Eq. (A2). ■

In light of Lemma 4, we may refer to a sliding trajectory as a *sliding front*. More generally, we make the following definition.

Definition 2. A *sliding front* is a smooth curve that everywhere satisfies Eq. (A1) or, equivalently, Eq. (A2).

Note that a sliding front may be composed of multiple trajectories joined at fixed points. Also, any segment of a sliding front is also referred to as a sliding front.

Lemma 5. BIMs are sliding fronts, and thus lie within the sliding surface.

Proof. A BIM is the unstable invariant manifold of an SSU burning fixed point. Since we consider time-independent flows, this invariant manifold is also a trajectory. As shown in Ref. [8], BIMs satisfy the front compatibility criterion. Therefore, by Lemma 4, BIMs are sliding fronts. ■

Since the sliding surface is invariant, it is natural to restrict Eq. (2) to this surface. We next derive an explicit expression for this 2D flow. Applying the sliding constraint (A1) to the front element dynamics (2), we have $\mathbf{u}\cdot\hat{\mathbf{n}} = -v_0$. Using this to resolve the unit vector $\hat{\mathbf{n}}$ into components, we have $\hat{\mathbf{n}}\cdot\hat{\mathbf{u}} = -v_0/|\mathbf{u}|$ and $\hat{\mathbf{n}}\cdot\hat{\mathbf{u}}^\perp = \mp\sqrt{1-(v_0/|\mathbf{u}|)^2}$, where $\mathbf{u}^\perp$ or $\hat{\mathbf{u}}^\perp$ is a right-handed rotation by $\pi/2$ of $\mathbf{u}$ or $\hat{\mathbf{u}} = \mathbf{u}/|\mathbf{u}|$. Inserting the resolved form of $\hat{\mathbf{n}}$ into Eq. (2), we have

$$\dot{\mathbf{r}} = \mathbf{w}_\pm \equiv \left[1-\left(\frac{v_0}{|\mathbf{u}|}\right)^2\right]\mathbf{u} \mp \frac{v_0}{|\mathbf{u}|}\sqrt{1-\left(\frac{v_0}{|\mathbf{u}|}\right)^2}\,\mathbf{u}^\perp. \tag{A3}$$

This defines two flows over the fast zone, one for each of the two branches of the sliding surface. Our sign convention is such that $\mathbf{w}_+$ is the flow on the branch where $\dot{\mathbf{r}} = +|\dot{\mathbf{r}}|\hat{\mathbf{g}}$ (the $+$ branch), and $\mathbf{w}_-$ is the flow on the branch where $\dot{\mathbf{r}} = -|\dot{\mathbf{r}}|\hat{\mathbf{g}}$ (the $-$ branch).

Equation (A3) shows that the $\mathbf{w}_\pm$ fields are undefined (complex valued) within the slow zone and are zero on its boundary, confirming Lemma 1. All fixed points of Eq. (2) are fixed points of Eq. (A3) because all burning fixed points trivially satisfy the sliding constraint. These burning fixed points lie on the slow zone boundary. Equation (A3) also has a set of spurious fixed points at all other points along the slow zone boundary, i.e., where $|\mathbf{u}| = v_0$. However, we ignore these spurious fixed points as they are not physically relevant fixed points of Eq. (2), but rather result from the square-root singularity in Eq. (A3), obtained by projecting Eq. (2) onto xy space. This square-root singularity also invalidates the uniqueness of solutions to Eq. (A3) at the slow zone boundary. Thus, there are other physically relevant trajectories that pass through the slow zone boundary.

Figures 22(b) and 22(d) and 23(b) and 23(d) illustrate the $\mathbf{w}_\pm$ flows for the cases of hyperbolic and elliptic fluid flow, respectively. The gray regions are the slow zones. burning fixed points are indicated on the boundary of the hyperbolic slow zone. The stable and unstable manifolds of these burning fixed points are shown in blue and red, respectively.

Reference [8] proved that for any burning fixed point, $\hat{\mathbf{g}}$ is an eigenvector of $u_{i,j}$, i.e.,

$$u_{i,j}\hat{g}_j = \mu\hat{g}_i, \tag{A4}$$

where μ is the eigenvalue. Reference [8] also defined the quantity μ',

$$\mu' = \mu + v_0\kappa, \tag{A5}$$

where κ is the signed curvature of the slow zone boundary at the burning fixed point. ($\kappa < 0$ means that $\hat{\mathbf{n}}$ points toward the center of curvature.) Following, we reproduce Theorem 4 from Ref. [8] [43]:

Theorem 1. For a time-independent, incompressible flow $\mathbf{u}$, the eigenvalues about a burning fixed point are

$$\lambda_0 = -\mu, \tag{A6}$$

$$\lambda_\pm = \tfrac{1}{2}(-\mu \pm \sqrt{\mu^2 + 4\mu\mu'}), \tag{A7}$$

where μ and μ' are given by Eqs. (A4) and (A5). The linear stability of a burning fixed point is thus determined by the signs of μ and μ' according to the following table:

	$\mu > 0$	$\mu < 0$
$\mu' > 0$	SUS	UUU
$\mu' < 0$	SSS	SUU

We next specialize this result to the dynamics on the sliding surface.

Corollary 1. The eigenvalues for a burning fixed point of the dynamics (2) restricted to the sliding surface are given by $\lambda_\pm$ from Eq. (A7). The xy projection of each of the corresponding eigenvectors is proportional to $\hat{\mathbf{g}}$.

The sliding surface stability information is summarized in Fig. 24. For each of the four stability types, the first two stabilities (in bold) describe the dynamics within the invariant sliding surface. Equation (A5) places restrictions on the local convexity of the slow zone at the burning fixed point. These possibilities are illustrated in Fig. 24.

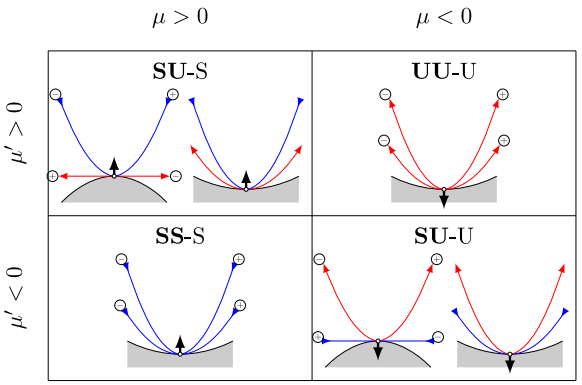

FIG. 24. (Color online) Four burning fixed point stability types. Black arrow indicates burning direction. Gray regions are slow zones. Two unstable (stable) manifolds of each burning fixed point are within the sliding surface. Each manifold is labeled with $+/-$ indicating its corresponding branch of the sliding surface.

Lemma 6. At an intersection $\mathbf{p}$ between a sliding front and the boundary of a slow zone, the fluid flow is perpendicular to the sliding front. If the sliding front is tangent to the boundary, $\mathbf{p}$ is a burning fixed point. Otherwise, $\mathbf{p}$ is a cusp along the sliding trajectory. All burning fixed points and cusps of sliding fronts occur at the intersection between a sliding front and slow zone boundary.

Proof. Combining the sliding constraint Eq. (A1) with the front element dynamics (2) gives $\mathbf{u}\cdot\hat{\mathbf{n}} = -v_0$. Since $|\mathbf{u}| = v_0$ on the slow zone boundary, $\mathbf{u} = -v_0\hat{\mathbf{n}}$. Thus, $\mathbf{u}$ is perpendicular to $\hat{\mathbf{g}}$. In Theorem 2 of Ref. [8], it was shown that a necessary and sufficient condition for a burning fixed point was for it to be on the boundary of the slow zone with $\hat{\mathbf{n}}$ perpendicular to the boundary. Thus, $\hat{\mathbf{g}}$ tangent to the boundary implies a burning fixed point. If $\hat{\mathbf{g}}$ is not tangent to the boundary, then since the sliding trajectory cannot enter the slow zone, it reaches the boundary and then must reverse direction forming a cusp. Finally, a burning fixed point and cusp both require $\dot{\mathbf{r}} = 0$. This satisfies the sliding constraint and also implies $|\mathbf{u}| = v_0$. ■

Lemma 7. A burning fixed point or cusp on the boundary of the fluid domain, i.e., at a wall, must have $\hat{\mathbf{g}}$ perpendicular to that boundary.

Proof. This follows from the previous Lemma 6 and that the fluid velocity of an incompressible fluid is tangent to the fluid domain boundary.

An incompressible 2D fluid flow can be specified by a stream function $\Psi(\mathbf{r})$, with $u_x = d\Psi/dy$, $u_y = -d\Psi/dx$. Each fluid element follows a level set, or streamline, of Ψ. Front elements, on the other hand, do not follow streamlines, but generally cross them one way or the other depending on their relative orientation.

Lemma 8. Sliding fronts cross streamlines such that $\theta_{\hat{\mathbf{n}},\mathbf{u}}$, the angle between $\hat{\mathbf{n}}$ and $\mathbf{u}$, satisfies $\cos(\theta_{\hat{\mathbf{n}},\mathbf{u}}) = -v_0/|\mathbf{u}|$.

Proof. From Eq. (2), $\mathbf{u} = \dot{\mathbf{r}} - v_0\hat{\mathbf{n}}$. The sliding front condition implies $\mathbf{u} = \pm|\dot{\mathbf{r}}|\hat{\mathbf{g}} - v_0\hat{\mathbf{n}}$. Dotting with $\hat{\mathbf{n}}$, $\hat{\mathbf{n}}\cdot\mathbf{u} = -v_0$.■

Lemma 8 means that sliding fronts are never tangent to streamlines, except in the $v_0/|\mathbf{u}| \to 0$ limit. Physical boundaries of the fluid (channel walls) are particularly important streamlines at which this lemma can be utilized.

In addition to the angle at which sliding fronts cross streamlines, we can examine how rapidly they are crossed. To this end, we calculate the rate at which Ψ changes when viewed from the frame of an individual front element

$$\frac{D\Psi}{Dt} \equiv \frac{\partial\Psi}{\partial x}\frac{\partial x}{\partial t} + \frac{\partial\Psi}{\partial y}\frac{\partial y}{\partial t} + \frac{\partial\Psi}{\partial t} \tag{A8}$$

$$= -u_y\dot{x} + u_x\dot{y} \tag{A9}$$

$$= -(\dot{y} + v_0\cos\theta)\dot{x} + (\dot{x} - v_0\sin\theta)\dot{y} \tag{A10}$$

$$= -v_0\dot{\mathbf{r}}\cdot\hat{\mathbf{g}} \tag{A11}$$

$$= -\operatorname{sgn}(\dot{\mathbf{r}}\cdot\hat{\mathbf{g}})v_0|\dot{\mathbf{r}}|, \tag{A12}$$

where the last equality makes use of the sliding constraint. Scaling by the front element speed, we find the simple relation

$$\frac{D\Psi}{Ds} = -\operatorname{sgn}(\dot{\mathbf{r}}\cdot\hat{\mathbf{g}})v_0, \tag{A13}$$

where s measures the Euclidean xy length along the trajectory. Equation (A13) shows that the sliding trajectories on the $+$ ($-$) branch of the sliding surface are those that climb the stream function with the constant rate of descent (ascent) v_0. It is straightforward to show that the only front elements that ascend or descend at a constant rate are sliding.

Consider two streamlines with values Ψ_a and Ψ_b and a sliding front $F_{a,b}$ that connects one to the other with no intervening cusps. The xy length of the segment $F_{a,b}$ follows directly from Eq. (A13):

$$|F_{a,b}| = \frac{|\Psi_b - \Psi_a|}{v_0}. \tag{A14}$$

This expression is particularly useful when thinking about frozen fronts in channel flows of arbitrary geometry. Since the channel wall enforces a boundary condition of constant Ψ, the frozen front length is found through Eq. (A14). Thus, the length of a frozen front that spans a channel depends only on this "energy difference" between the two walls and the burning speed, and not on other details of the flow. While Eq. (A14) was derived for a single sliding front, it also holds for frozen fronts that are composed of multiple BIM cores. This can be seen by applying Eq. (A14) to each BIM segment separately. Interestingly, this implies that multiple frozen fronts existing in the same flow must have the same length, even in the absence of any flow symmetry.

Equation (A14) also implies that a channel of width W cannot support a frozen front if $\Delta\Psi < v_0 W$. Furthermore, if we assume that a flow $\mathbf{u}$ *without* wind gives no net flow down the channel, then for the flow $\mathbf{u} + \mathbf{v}_w$, Eq. (A14) becomes

$$|F_{a,b}| = W v_w / v_0. \tag{A15}$$

This can be interpreted as the equality of fluid flux across the frozen front and across the channel width. Equation (A15) shows that $v_w \geqslant v_0$ is necessary but not sufficient. In the case that frozen fronts do occur at $v_w = v_0$, they must be straight lines that meet the channel walls at right angles. This occurs exactly when the original fluid flow ($v_w = 0$) has a vertical advective separatrix. This condition is met for the windy alternating vortex chain model; additionally, Ref. [10] experimentally demonstrated that $v_w = v_0$ marked the onset of frozen fronts. However, it is not difficult to construct flows where $v_w = v_0$ is not sufficient for the existence of frozen fronts.

APPENDIX B: STABILITY OF FROZEN DOMAINS

At the beginning of Sec. IV, we specified that frozen domains should be stable under small perturbations. Here, we define this stability more precisely. For a given invariant burned domain, with boundary F, we define an *allowable* distortion of F at a point $\mathbf{r} \in F$ to be a distortion such that F remains unchanged outside a ball of radius $\epsilon(\mathbf{r}) > 0$ centered at $\mathbf{r}$. Note that the value of $\epsilon(\mathbf{r})$ is not fixed but may vary with the point $\mathbf{r}$.

Definition 3 (Stability of frozen domains and fronts). A frozen domain (front) is required to be *stable* in the following sense. There must exist a function $\epsilon(\mathbf{r})$ of each point $\mathbf{r}$ along the front F, i.e., the domain boundary, such that after any allowable distortion, the front remains pointwise close to F and converges pointwise to F as time goes to infinity.

Here, pointwise close is in the "Lyapunov" sense, in that the maximum (over all time) distance from the time-evolved distorted front to the original front F remains bounded and goes to zero as ϵ goes to zero.

With this definition, one can easily verify the argument of Sec. IV proving that a frozen front cannot contain an SUU or UUU burning fixed point. One also sees that a frozen front can contain an SSU or SSS burning fixed point, and that the curves constructed in Proposition 1 are stable. Regarding the latter, it is interesting to note how a perturbation of the frozen front F returns to F. First, a perturbation localized to the neighborhood of an SSS point simply shrinks in size, back into the original frozen front, due to the SSS point's being a sink. Consider now a perturbation localized at some point $\mathbf{r}$ of the frozen front that is not an SSS burning fixed point. This perturbation will be "swept" along the front, away from

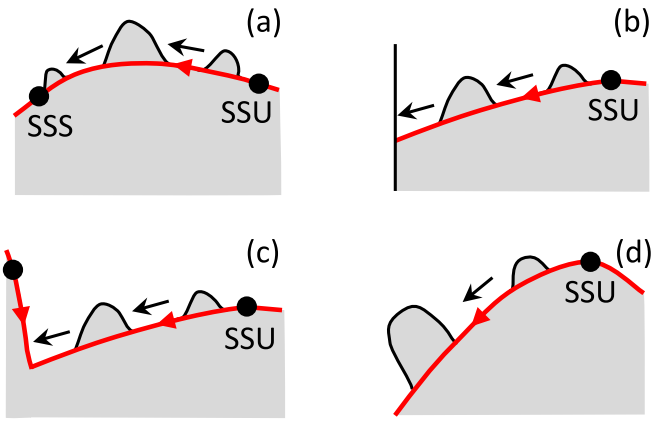

FIG. 25. (Color online) The fates of localized perturbations to a frozen front. (a) The perturbation eventually shrinks into an SSS burning fixed point on the frozen front. (b) The perturbation strikes a wall of the fluid domain. (c) The perturbation strikes a second BIM core at a concave corner of the frozen front. (d) The perturbation goes to infinity along a BIM core that stretches to infinity. Although the size of the perturbation could grow indefinitely, the perturbed front still returns to the frozen front pointwise.

the unstable burning fixed point that generates the BIM; the perturbation might even initially grow in size. The localized perturbation will continue to follow the BIM segment from which it was perturbed, and will subsequently encounter either an SSS point, a domain wall, another BIM segment of the frozen front, or it will be swept to infinity (Fig. 25). In the initial three cases, it is clear that the perturbation will disappear as it either shrinks into the SSS burning fixed point [Fig. 25(a)], strikes the wall [Fig. 25(b)], or runs into the already burned region [Fig. 25(c)], assuming the initial size of the perturbation $\epsilon(\mathbf{r})$ is sufficiently small. The case in which the perturbation is swept to infinity [Fig. 25(d)] requires an additional assumption on the far-field nature of the fluid flow which we will address in a future publication.

[1] T. John and I. Mezic, Phys. Fluids **19**, 123602 (2007).
[2] D. Beule, A. Förster, and T. Fricke, Z. Phys. Chem. **204**, 1 (1998).
[3] A. Scotti and J. Pineda, J. Marine Res. **65**, 117 (2007).
[4] I. Prigogine and I. Stengers, *Order Out of Chaos: Man's New Dialogue with Nature* (Bantam, New York, 1984).
[5] A. Babloyantz, *Molecular Dynamics and Life: An Introduction to Self-Organization of Matter* (Wiley, New York, 1986).
[6] C. A. Russell, D. L. Smith, L. A. Waller, J. E. Childs, and L. A. Real, Proc. R. Soc. London, Ser. B **271**, 21 (2004).
[7] J. Mahoney, D. Bargteil, M. Kingsbury, K. Mitchell, and T. Solomon, Europhys. Lett. **98**, 44005 (2012).
[8] K. A. Mitchell and J. Mahoney, Chaos **22**, 037104 (2012).
[9] D. Bargteil and T. Solomon, Chaos **22**, 037103 (2012).
[10] M. E. Schwartz and T. H. Solomon, Phys. Rev. Lett. **100**, 028302 (2008).
[11] S. Chandresekhar, *Hydrodynamic and Hydromagnetic Stability* (Clarendon Press, Oxford, 1961).
[12] R. M. Clever and F. H. Busse, J. Fluid Mech. **65**, 625 (1974).
[13] E. W. Bolton, F. H. Busse, and R. M. Clever, J. Fluid Mech. **164**, 469 (1986).
[14] T. H. Solomon and J. P. Gollub, Phys. Rev. A **38**, 6280 (1988).
[15] M. C. Cross and P. C. Hohenberg, Rev. Mod. Phys. **65**, 851 (1993).
[16] D. Etling and R. A. Brown, Boundary-Layer Meteor. **65**, 215 (1993).
[17] B. W. Atkinson and J. W. Zhang, Rev. Geophys. **34**, 403 (1996).
[18] B.I. Shraiman, Phys. Rev. A **36**, 261 (1987).
[19] T. Solomon and J. Gollub, Phys. Fluids **31**, 1372 (1988).
[20] R. Camassa and S. Wiggins, Phys. Rev. A **43**, 774 (1991).
[21] T. H. Solomon, S. Tomas, and J. L. Warner, Phys. Rev. Lett. **77**, 2682 (1996).
[22] M. Abel, A. Celani, D. Vergni, and A. Vulpiani, Phys. Rev. E **64**, 046307 (2001).
[23] M. Abel, M. Cencini, D. Vergni, and A. Vulpiani, Chaos **12**, 481 (2002).
[24] M. Cencini, A. Torcini, D. Vergni, and A. Vulpiani, Phys. Fluids **15**, 679 (2003).
[25] M. S. Paoletti and T. H. Solomon, Europhys. Lett. **69**, 819 (2005).
[26] M. S. Paoletti and T. H. Solomon, Phys. Rev. E **72**, 046204 (2005).
[27] J. R. Boehmer and T. H. Solomon, Europhys. Lett. **83**, 58002 (2008).
[28] S. K. Scott, *Oscillations, Waves, and Chaos in Chemical Kinetics* (Oxford University Press, Oxford, 1994).
[29] A. Pocheau and F. Harambat, Phys. Rev. E **73**, 065304 (2006).
[30] A. Pocheau and F. Harambat, Phys. Rev. E **77**, 036304 (2008).
[31] Z. Neufeld and E. Hernandez-Garcia, *Chemical and Biological Processes in Fluid Flows: A Dynamical Systems Approach* (Imperial College Press, London, 2009).
[32] There are small variations in the propagation speed due to curvature of the reaction front, but this effect is minimal in these experiments.
[33] The experiment presented here depends on a redox reaction, and in this spirit we use the term "burning" to refer to any similar form of front propagation.
[34] G. B. Jeffery, Proc. R. Soc. London, Ser. A **102**, 161 (1922).
[35] M. Oberlack and A. F. Cheviakov, J. Eng. Math. **66**, 121 (2010).
[36] These frozen domains are similar to the minimal forward invariant sets studied in the context of random differential equations with bounded noise [44,45].
[37] T. H. Solomon and I. Mezić, Nature (London) **425**, 376 (2003).
[38] E. Hernandez-Garcia and C. Lopez, Ecol. Complexity **1**, 253 (2004).
[39] M. Kaern and M. Menzinger, J. Phys. Chem. B **106**, 3751 (2002).
[40] S. Saha, S. Atis, D. Salin, and L. Talon, Europhys. Lett. **101**, 38003 (2013).
[41] P. W. Megson, M. L. Najarian, K. E. Lilienthal, and T. H. Solomon, Phys. Fluids **27**, 023601 (2015).
[42] Interestingly, these two sliding surfaces are related by $x \leftrightarrow y$ symmetry.
[43] We correct a typo in the original: in the bottom row of the table, $\mu' > 0$ now reads as $\mu' < 0$.
[44] A. J. Homburg and T. R. Young, Topol. Methods Nonlin. Anal. **35**, 77 (2010).
[45] J. S. W. Lamb, M. Rasmussen, and C. S. Rodrigues, Proc. Am. Math. Soc. (to be published) (arXiv:1105.5018).